Mechanics of Materials 142 (2020) 103296

Contents lists available at ScienceDirect

Mechanics of Materials

journal homepage: www.elsevier.com/locate/mechmat

Research paper

X-ray computed tomography investigation of dilation of mineral-filled PVC under monotonic loading

Sindre Nordmark Olufsen*[a], Arild Holm Clausen[a], Dag Werner Breiby[b], Odd Sture Hopperstad[a]

[a] Structural Impact Laboratory (SIMLab), Department of Structural Engineering, NTNU, Norwegian University of Science and Technology, Trondheim NO-7491, Norway
[b] PoreLab, Department of Physics, NTNU, Norwegian University of Science and Technology, Trondheim NO-7491, Norway

ARTICLE INFO

Keywords:
Polyvinyl chloride
PVC
X-ray computed tomography
Triaxiality
Strain rate
Digital image correlation
Tensile test
Volume change

ABSTRACT

The deformation-induced dilation of mineral-filled polyvinyl chloride (PVC) is investigated by means of polychromatic X-ray absorption tomography (XCT). Axisymmetric notched tensile specimens are strained to prescribed elongations using a tensile test apparatus and subsequently scanned by XCT after relaxation. During straining, surface deformations are quantified by digital image correlation (DIC) and contour tracking. The influence of stress triaxiality and strain rate on dilation is investigated by using tensile specimens with three different notch radii, all strained to three deformation levels at two different nominal strain rates. Pronounced reduction of density, corresponding to an increase of volume, is observed for all specimens in the XCT scans, but markedly different relative density distributions are measured for the three geometries. The accuracy of the polychromatic XCT density estimates is evaluated against data obtained with monochromatic synchrotron radiation computed tomography (sr-XCT), and a comparison to surface deformation-based dilation estimates is presented.

1. Introduction

When designing structural components made of polymeric materials, the assessment of their structural integrity can be a challenge. Finite element analysis has become the standard tool for this task, but the credibility of the results is strongly dependent on the material model's ability to describe the mechanical behavior of the material at hand. Material models suitable for polymers are found in abundance in the literature, and the available models vary significantly in complexity, see for example Bergström (2015). As most polymeric materials are rate sensitive, viscoelastic and viscoplastic models are typically employed. Further, plastic dilation in the form of voids or crazes has been reported for both semi-crystalline and amorphous polymeric materials, in several cases indicating void volume fractions reaching tens of percent (Boisot et al., 2011; Laiarinandrasana et al., 2012; Poulet et al., 2016; Brusselle-Dupend et al., 2011; Ognedal et al., 2014b; 2014a). Including dilation in material models is important, as this feature will influence plastic flow, strain localization, geometrical changes and thereby the failure behavior of the component.

It can be a challenging task to measure the dilation within a material. Numerous techniques such as specific density measurements, surface-deformation based estimates (Ognedal et al., 2014a; Johnsen et al., 2017; G'Sell et al., 2002), scanning electron microscopy (SEM) (Ognedal et al., 2014a; Boisot et al., 2011) and X-ray computed tomography (XCT)(Laiarinandrasana et al., 2012; Poulet et al., 2016; Brusselle-Dupend et al., 2011; Bø Fløystad et al., 2015; Esmaeili et al., 2013; Diaz et al., 2012) have been applied. Light microscopy and SEM are especially useful for investigation of fracture surfaces, and sub-micron sized features can be resolved by using SEM (Ognedal et al., 2014a; Johnsen et al., 2017).

X-ray computed tomography is a particularly attractive technique as non-destructive spatial density measurements are possible, provided that excessive radiation damage is avoided (Maire and Withers, 2014). XCT has been used in numerous studies, see for instance (Laiarinandrasana et al., 2012; Poulet et al., 2016; Brusselle-Dupend et al., 2011; Bø Fløystad et al., 2015; Esmaeili et al., 2013; Diaz et al., 2012), but has only recently been demonstrated as an in-situ technique for measuring density changes within a polymer specimen during tensile testing (Poulet et al., 2016; Brusselle-Dupend et al., 2011). Home laboratory X-ray CT apparatuses are widely available, but the long acquisition time, limited resolution and polychromatic nature of commonly used X-ray sources limit the applicability of such equipment (Hsieh, 2015). These limitations can be overcome by using synchrotron radiation X-ray computed tomography (sr-XCT), but there are comparatively few synchroton facilities and the beam-time is limited and expensive.

* Corresponding author.
E-mail address: sindre.n.olufsen@ntnu.no (S.N. Olufsen).

https://doi.org/10.1016/j.mechmat.2019.103296
Received 4 July 2019; Received in revised form 14 November 2019; Accepted 16 December 2019
Available online 19 December 2019
0167-6636/ © 2019 The Authors. Published by Elsevier Ltd. This is an open access article under the CC BY license (http://creativecommons.org/licenses/by/4.0/).

When home laboratory CT equipment is used, the long acquisition time usually only allows for *ex situ* measurements. Studies on deformed materials are therefore typically performed by deforming the specimen incrementally, acquiring a tomogram for each increment. The polychromatic nature of home laboratory X-ray sources introduces the beam-hardening artifact. This artifact originates from the energy-dependent X-ray absorption of the material, causing the lower energy X-rays to be more efficiently absorbed by the specimen. This artifact can be reduced by pre-hardening of the X-ray beam using filters, or by post-processing software corrections (Hsieh, 2015).

The spatial resolution and the scattering contrast define the length scales of the features that can be resolved within the polymer, and resolving sub-resolution voids is not feasible. "Local tomography" is a technique which allows first getting an overview of a large sample volume, before zooming-in to study specific regions of interest, and has been demonstrated to resolve the internal structures of interest in deformed specimens made of nylon PA6 (Laiarinandrasana et al., 2012; 2016). Another approach, which we will pursue in this article, is to exploit the proportionality between X-ray absorption and material density to measure material dilation. By performing XCT on a larger region of the specimen, the local void volume fraction can be deduced from the density distribution (Brusselle-Dupend et al., 2011). This method allows for void volume fraction measurements to cover larger regions, at the cost of losing information about the exact void morphology.

The tendency of a polymer to dilate during deformation is influenced by intrinsic properties such as inclusions (Ognedal et al., 2014b) and microstructure, and external factors such as stress state (Boisot et al., 2011; Ognedal et al., 2014b) as well as strain rate and temperature (Johnsen et al., 2017). In order to create a certain stress state at a material point, the geometry of the specimen can be tailored. Axisymmetric notched tensile specimens are widely applied for this purpose as they provide an analytically described stress field in their undeformed state.

When notched tensile specimens are employed, strain measurements are complicated by the inhomogeneous deformation of the specimen. Digital image correlation (DIC) has become a widely used tool, capable of performing local strain measurements beyond the point of strain localization (Sutton et al., 2009). When the deformation of the specimen surface has been quantified, an estimate of the volume increase of a section of the specimen can be obtained (Rossi et al., 2018; Andersen et al., 2019). Such estimates rely on assumptions regarding the internal deformation of the specimen, and do not necessarily yield valid results (Laiarinandrasana et al., 2016). One way to evaluate the accuracy of surface-based measurements of the volume change is to compare such data with density changes determined by computed tomography.

The objective of this study is twofold. Firstly, this study extends previous studies on mineral filled PVC (Ognedal et al., 2014b; 2014a; 2012; Andersen, 2016; Olufsen et al., 2019) by including spatial CT measurements of material dilation. Axisymmetric specimens with three notch geometries, giving different stress triaxiality in the notch region, are deformed to three different elongations at two strain rates. Local strain measurements beyond the point of localization are obtained by DIC and employed to determine the true stress-strain curves. Motivated by the increasing availability of home laboratory XCT equipment in the industry, an efficient methodology for spatial material dilation measurements using axisymmetric specimens is proposed and validated against sr-XCT. These measurements can be directly compared to finite element simulations, aiding further development of material models suitable for polymeric materials. Secondly, the accuracy of surface-deformation-based dilation estimates obtained with a digital camera is assessed by comparing the estimates to the XCT measurements. The surface-deformation-based approach can only provide information about the average change of volume through the cross-section, but is attractive due to its practicality.

The paper is organised as follows: materials and methods are outlined in Section 2, experimental results are presented in Section 3, and key findings are discussed in Section 4. The conclusions from the study are compiled in Section 5.

2. Materials and methods

2.1. Material

A mineral-filled polyvinyl-chloride (PVC) containing approx. 24vol % $CaCO_3$ particles is investigated in this study. The material is the same as previously investigated by Olufsen et al. (2019), and similar to the one investigated by Ognedal et al. (2014b) and Andersen (2016). Samples of the material were extracted from 10 mm thick extruded plates produced by Kömmerling. Two groups of particles have been identified in the material, being small spherical particles with a typical diameter in the range from 0.2 μm to 0.4 μm, and larger irregularly shaped particles (Olufsen et al., 2019).

2.2. Tensile specimens

Axisymmetric notched tensile specimens were employed in this study, allowing for manipulation of the initial stress triaxiality ratio in the notch region of the specimen. Motivated by the correlation between reduced notch radius and increased material dilation reported by Ognedal et al. (2014b) and Olufsen et al. (2019), three different notch radii of 20 mm, 5 mm and 2 mm were used, hereafter referred to as R20, R5 and R2 specimens, respectively. The specimens are illustrated in Fig. 1.

A cylindrical coordinate system with origin in the center of the minimum cross-section of the notch is defined, see Fig. 2.

According to finite element simulations assuming linear elastic material behavior, a notch radius of 20 mm, 5 mm or 2 mm gives an initial stress triaxiality ratio of approx. 0.4, 0.6 or 0.8, respectively, in the origin of the specimens (Ognedal et al., 2014b).

The specimens were fabricated from the extruded plates by turning, carefully avoiding bending and heating of the specimens. The extrusion direction of the plate was oriented coaxially with the longitudinal axis of the specimens. Fastening to the tensile test apparatus was done by threading of both ends of the specimens. Digital image correlation was

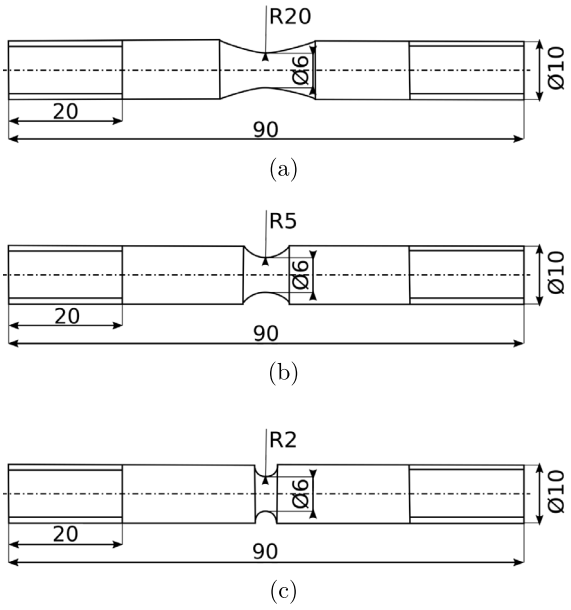

Fig. 1. Axisymmetric notched tensile specimens with a notch radius of 20 mm (a), 5 mm (b) and 2 mm (c). Units are in mm.

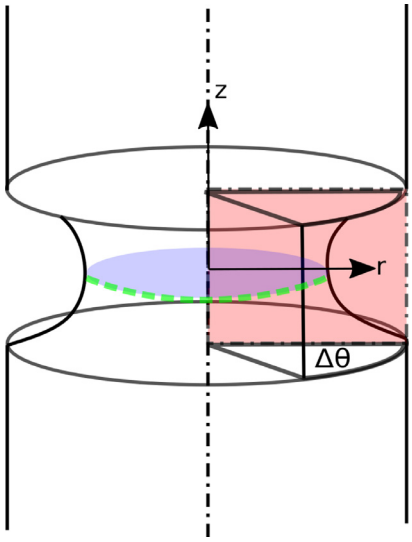

Fig. 2. Notch region of a specimen with a plane used for re-slicing the tomograms (red), the cross-sectional disc (blue) and the circumferential path (green) where strains are measured. (For interpretation of the references to colour in this figure legend, the reader is referred to the web version of this article.)

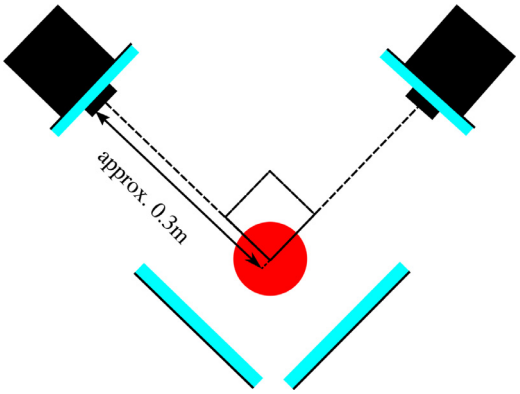

Fig. 3. Top view of experimental setup showing a tensile specimen (red), two orthogonal cameras (black) and additional lighting (cyan) surrounding the camera lenses and behind the specimen. Note that the sketch is not drawn to scale. (For interpretation of the references to colour in this figure legend, the reader is referred to the web version of this article.)

facilitated by applying dispersed paint to the surface of the specimen by using an airbrush, giving a speckle-like appearance of the surface.

2.3. Tensile test setup

The tensile tests were performed using an Instron 5082 tensile test machine equipped with a 2 kN load cell. Two Prosilica GC2450 cameras equipped with a Nikon 105 mm f/2.8G macro lens and a Sigma 105 mm F2.8 EX DG macro lens were used. An illustration of the experimental setup is shown in Fig. 3. One camera was aligned with the normal direction of the extruded plate from which the test specimens were fabricated, and the other aligned with the in-plane direction of the plate. An aperture of F/12 was used, ensuring a sufficient focus depth. The distance between each camera and the specimen was approx. 0.3 m.

The specimens were deformed to prescribed elongations and then unloaded. Three different elongations of 1.5 mm, 2.0 mm and 2.5 mm were investigated for each specimen geometry. These elongations were chosen such that a significant part of the material's stress-strain curve before failure is covered.

Two target nominal strain rates of $10^{-4}\,s^{-1}$ and $10^{-3}\,s^{-1}$ were chosen. The corresponding test machine cross-head velocity was determined using finite element analysis with a previously calibrated material model (Andersen, 2016). Based on these numerical simulations, an initial nominal strain rate of $10^{-4}\,s^{-1}$ was obtained by using cross-head velocities of $2.8{\cdot}10^{-3}$ mm s^{-1}, $3.2{\cdot}10^{-3}$ mm s^{-1} and $3.7{\cdot}10^{-3}$ mm s^{-1} for the R2, R5 and R20 specimens, respectively. These velocities were increased with a factor of ten to give an initial nominal strain rate of $10^{-3}\,s^{-1}$. The same cross-head velocities were used during the entire loading and unloading processes. After unloading, the specimens were stored for a month or longer, relaxing any residual stresses, before continuing with XCT. Olufsen et al. (2019) provide further details and discussion of the experimental setup used to deform the tensile specimens.

2.4. DIC measurements

Digital image correlation was used to quantify surface deformation within the notched section of the specimen. Combined with force measurements from the tensile test apparatus, true stress vs true strain curves can be obtained. By using the deformation field along the circumference of the notch root, the volume change of a disc through the minimum cross-section of the notch root was estimated.

2.4.1. Measurement of strain, stress and surface curvature

Herein, the reported strain measure is the average longitudinal true strain along the visible circumference of the notch root, and the reported stress measure is the average longitudinal true stress in the minimum cross-section of the notch. Deformation of the specimen surface was quantified for the two cameras separately using an in-house B-spline-based 2D DIC code. A mesh convergence study was conducted by reducing the inter-nodal spacing until no further increase in strain was obtained. The typical inter-nodal spacing of a mesh used in the further analysis is in the order of 60 pixels. Using the approach described by Sutton et al. (2009), spurious longitudinal strains due to out of plane motion have been assessed for a corresponding experimental setup using the same material, being in the order of 0.002 (Olufsen et al., 2019).

The true strain components ε_j are calculated from the corresponding stretch ratios λ_j determined by the DIC code as:

$$\varepsilon_j = \ln(\lambda_j) \tag{1}$$

where the subscript j denotes the indices r, c and l, referring to the radial, circumferential and longitudinal direction, respectively. Olufsen et al. (2019) give a detailed presentation of the procedure used to determine these strain components. The average longitudinal true strain in the notch root is calculated as the average value of ε_l along the visible circumferential path as indicated with the dashed green line in Fig. 2. This average longitudinal true strain is hereafter referred to as the true strain.

The longitudinal true stress in the minimum cross-section of the notch is determined by:

$$\sigma = \frac{4F}{\pi d^2} \tag{2}$$

where F is the force measured by the load cell and d is the diameter of the minimum cross-section of the notch, which was continuously monitored by DIC. The diameter was determined by the 2D DIC routine as $d = \lambda_r d_0$ where λ_r is the average radial stretch of the minimum cross-section of the notch and d_0 is the initial diameter, see Olufsen et al. for further discussion (Olufsen et al., 2019). The average value of the measured diameter from the two cameras was used in Eq. (2).

The values of d obtained by DIC were verified by comparing with the diameter measured by an edge tracing routine. The curvature κ of the notch root was also obtained from the images by extracting the contour of the specimen for each frame. In the edge tracing routine, a circle was fitted to the notch root by means of a non-linear least squares method. The circle radius and its position along the longitudinal axis of

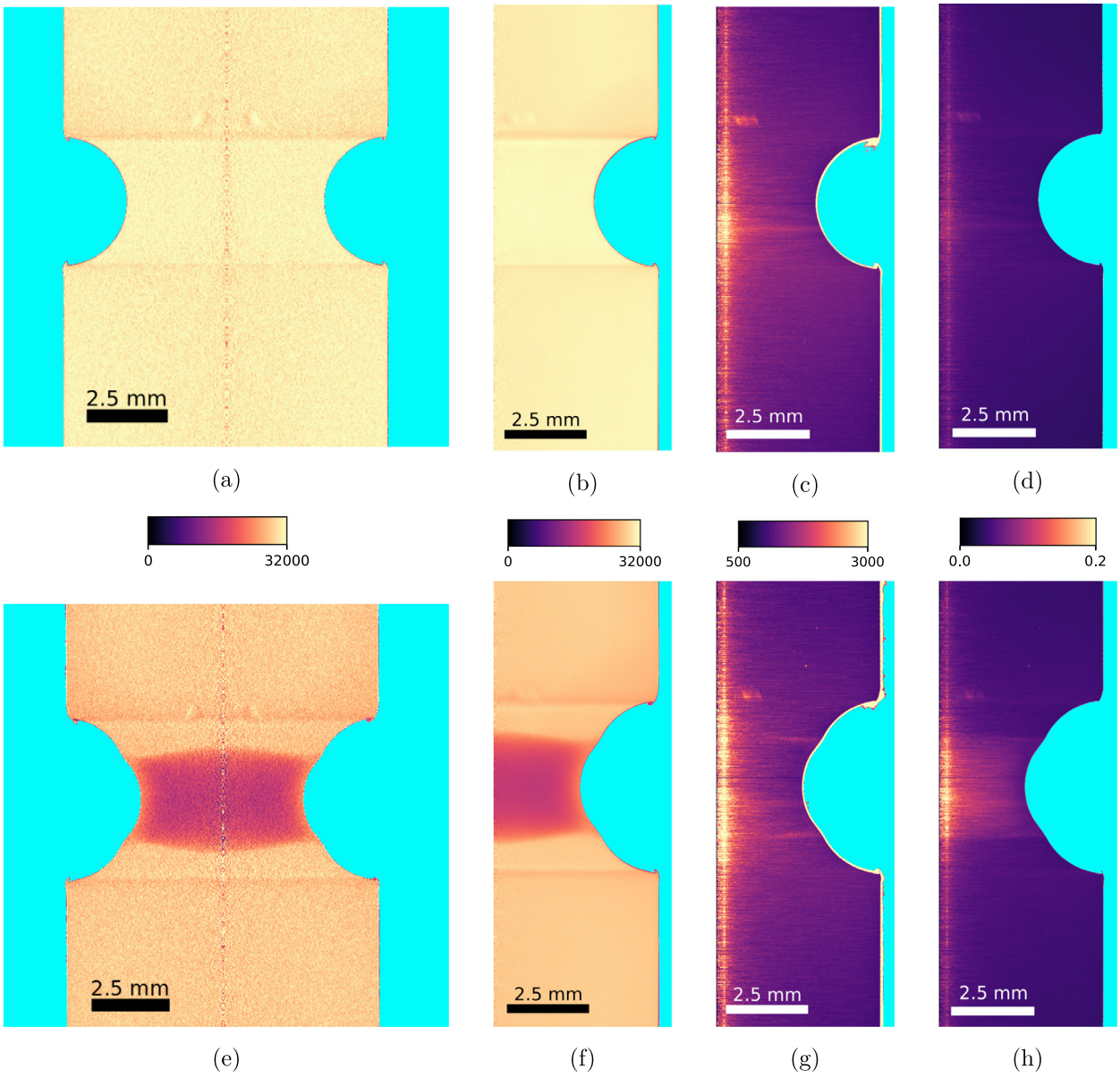

Fig. 4. Results obtained for each step of the procedure used to verify the assumption of axisymmetry for an undeformed (a-d) and elongated (e-h) R2 specimen. (a,e) Grey scale field $\xi(r, \theta, z)$ for one arbitrary value of θ, (b,f) average value $\mu_{\xi}(r, z)$ of the radial planes, (c,g) standard deviation $\sigma_{\xi}(r, z)$ of the radial planes, and (d,h) coefficient of variation $C_{v\xi}(r, z)$. The noisy appearance of the central axis in the field plots (a,e) is an artifact related to the axis of rotation in the XCT apparatus. The background is shown in cyan. (For interpretation of the references to colour in this figure legend, the reader is referred to the web version of this article.)

the specimen were used as optimization parameters.

2.4.2. Material dilation estimates based on surface deformations

A classical way of measuring material dilation is to estimate the volume change of a disc through the minimum cross-section of the notch root. A common measure of the volume change is the volume ratio $\lambda_V = \lambda_l \lambda_r^2$, where λ_l is the longitudinal stretch and λ_r is the radial stretch along the perimeter of the disc. The position of the disc is illustrated in Fig. 2. For easier comparison to the XCT measurements, however, the average relative density of the disc ρ^*_{disc} is the reported metric in this study. By assuming conservation of mass, ρ^*_{disc} is the inverse of the volume ratio λ_V, and is calculated as:

$$\rho^*_{disc} = \frac{1}{\lambda_l \lambda_r^2} \tag{3}$$

where λ_l and λ_r were obtained using DIC. In a similar fashion as in Eq. (2), λ_l and λ_r were measured by both cameras and the average value of the measurements was used in Eq. (3).

Eq. (3) assumes that the disc is flat and remains flat during deformation, which may not always be the case. An extension to Eq. (3) has been proposed by Andersen et al. (2019), accounting for the warping of the top and bottom surface of the disc:

$$\rho^*_{disc} = \frac{1}{\lambda_l \lambda_r^2 (\frac{r\Delta\kappa}{4} + 1)} \tag{4}$$

where r is the radius of the current minimum cross-section of the notch root as obtained by DIC, and $\Delta\kappa$ is the change in notch root curvature relative to the curvature of the undeformed specimen. Edge tracing of each frame was used to determine $\Delta\kappa$.

2.5. Material dilation from X-ray computed tomography (XCT)

The spatial relative density distribution within the notch region of all specimens was obtained with XCT after unloading. In addition, two

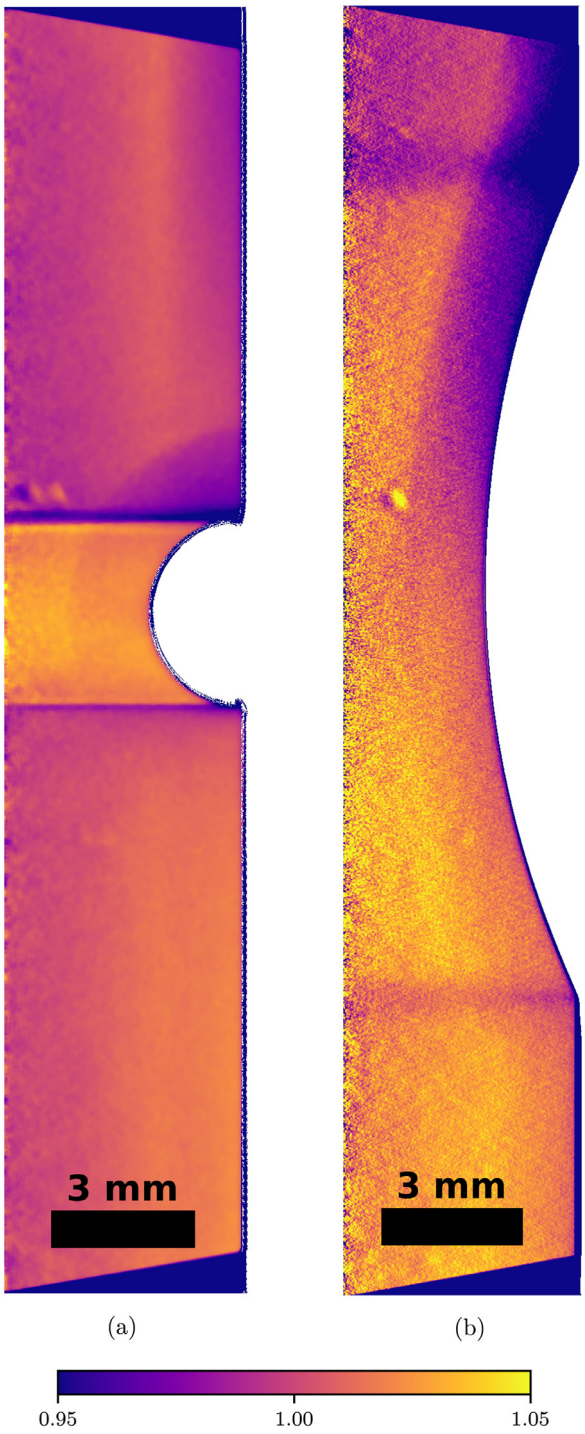

Fig. 5. Relative density calculated by Eq. (8) of a homogeneous and undeformed (a) R20 and (b) R2 specimen measured with XCT.

undeformed R20 and R2 specimens were also scanned. A Nikon XT H 225 ST μ-CT instrument equipped with a 16-Bit Perkin Elmer 1620 CN CS sensor and a tungsten reflection target was used for all scans. The polychromatic X-rays emitted by the source are used in a classical cone-beam geometry. In order to minimize the effect of beam hardening, a relatively high accelerator voltage of 160 kV was chosen, and a 0.2 mm copper filter was used to pre-harden the beam (Hsieh, 2015). The field of view was chosen such that the entire notch region of the specimen was visible, yielding a voxel size of 13.6 µm. It should here be emphasized that the discrete voids contained within the specimens are not resolved, and that the void volume fraction of each voxel is deduced

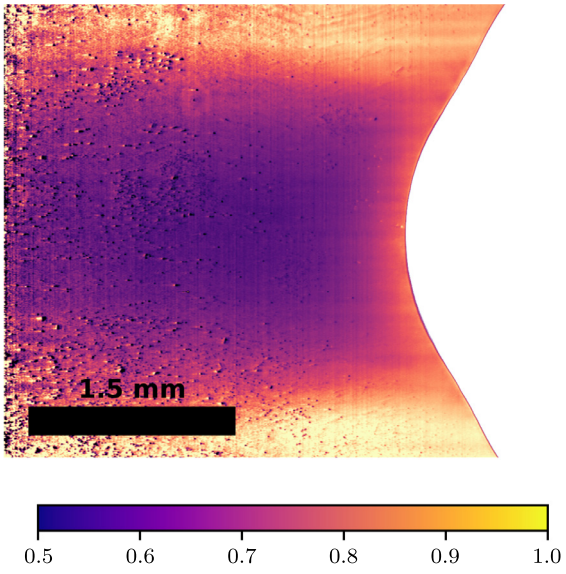

Fig. 6. Relative density field for the most elongated R2 specimen measured by sr-XCT. The spots are caused by dust on the scintilator.

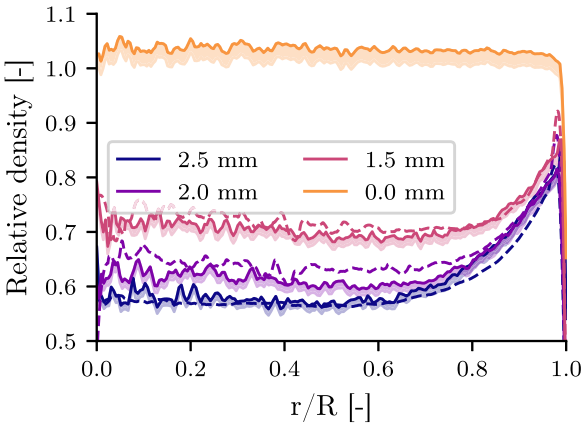

Fig. 7. Relative density vs. normalised radius for an un-elongated R2 specimen and specimens elongated by 0.0 mm, 1.5 mm, 2.0 mm, and 2.5 mm, acquired by XCT (solid line) and sr-XCT(dashed line). A shaded band is included for illustrating the consequence of increasing the reference grey scale value $\bar{\xi}$ by 3%. As the sr-XCT and XCT scans have slightly different voxel sizes, the radial coordinates are normalized to the minimum cross-sectional radius R. No sr-XCT scan is available for the undeformed specimen.

from the relative density of the voxel. During the acquisition of one tomogram, 3143 projections were captured. Reconstruction of the tomogram was done with the software Nikon Ct-Pro. The tomogram $\xi(x, y, z)$ was resampled into a cylindrical coordinate system and is hereafter treated as a continuous grey scale field $\xi(r, \theta, z)$, where inter-voxel values were determined by linear interpolation.

In order to reduce the noise level of the measurements, the axisymmetric nature of the specimens and the grey scale fields $\xi(r, \theta, z)$ was exploited. Assuming that the material is isotropic, the axisymmetry implies that the density field in all $r - z$ planes of the specimens should be identical. Any deviation between the $r - z$ planes should therefore be caused by noise. If the noise is of Gaussian nature, the average of all $r - z$ planes should contain a reduced noise level. Motivated by the cylindrical symmetry, the tomograms were re-sampled into a number of $r - z$ planes, spaced by an angular increment $\Delta\theta$, as shown in Fig. 2. The angular increment $\Delta\theta$ was chosen such that one new pixel was sampled at the perimeter of the section with the largest diameter for each increment. The re-sampling procedure was performed using a

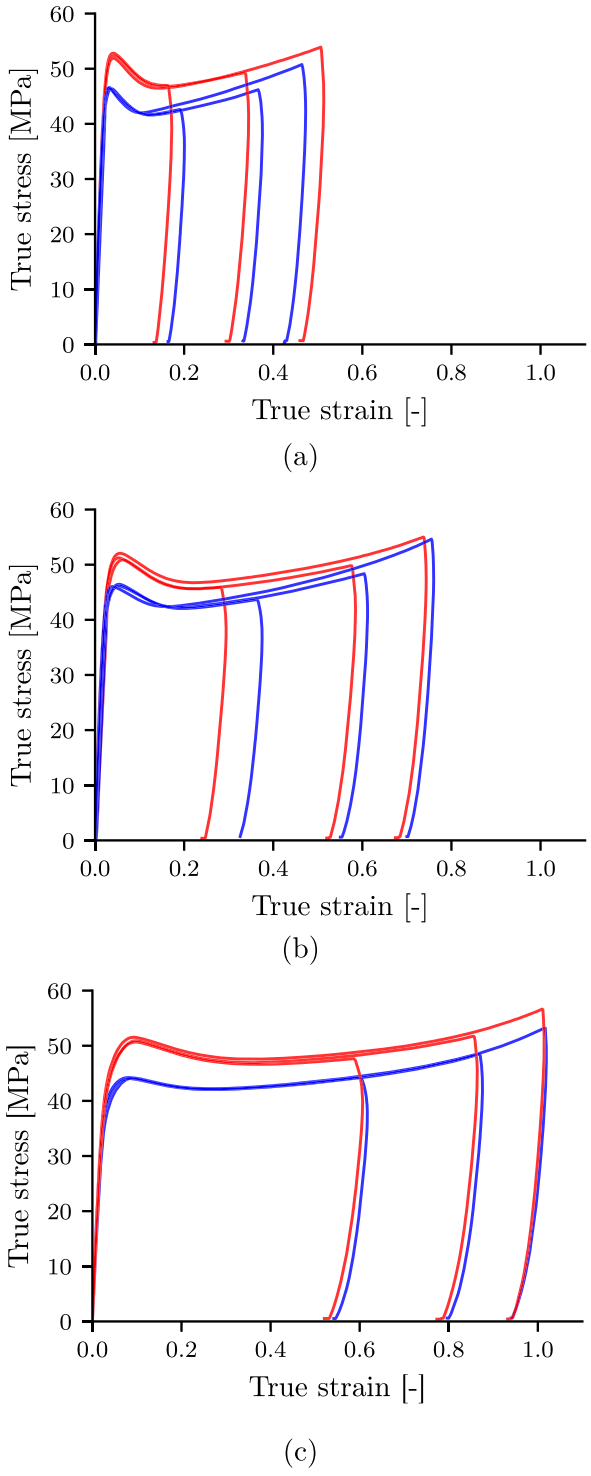

Fig. 8. True stress vs. true strain curves at minimum cross section at two nominal strain rates of $10^{-4}\,s^{-1}$ (blue) and $10^{-3}\,s^{-1}$(red) for specimens (a) R20, (b) R5, and (c) R2. (For interpretation of the references to colour in this figure legend, the reader is referred to the web version of this article.)

custom script and the image processing software Fiji (Schindelin et al., 2012). The average value $\mu_\xi(r, z)$ of the grey scale field $\xi(r, \theta, z)$ over all $r-z$ planes was then calculated as:

$$\mu_\xi(r, z) = \frac{1}{N}\sum_{i=1}^{N} \xi(r, \theta_i, z) \tag{5}$$

where $N \approx 2300$ is the number of angular increments. The corresponding standard deviation $\sigma_\xi(r, z)$ is given by:

$$\sigma_\xi(r, z) = \sqrt{\sum_{i=1}^{N} \frac{(\xi(r, \theta_i, z) - \mu_\xi(r, z))^2}{N}} \tag{6}$$

and the coefficient of variation $C_{v\xi}(r, z)$ was calculated as

$$C_{v\xi}(r, z) = \frac{\sigma_\xi(r, z)}{\mu_\xi(r, z)} \tag{7}$$

In order for $\mu_\xi(r, z)$ to be representative for the specimen, the density fields have to fulfil the assumption of axisymmetry even after large deformations. The following procedure was used to identify deviation from axisymmetry:

1. Reconstruct the tomogram $\xi(r, \theta, z)$
2. Re-sample the tomogram into a set of radial planes $\xi(r, \theta_i, z)$
3. Calculate $\mu_\xi(r, z)$ and $\sigma_\xi(r, z)$ with Eqs. (5) and (6), respectively
4. Based on $\mu_\xi(r, z)$ and $\sigma_\xi(r, z)$, calculate $C_{v\xi}(r, z)$ with Eq. (7)

The coefficient of variation $C_{v\xi}(r, z)$ should approach zero if there is no noise in the tomogram and the specimens are axisymmetric.

The procedure was applied to an undeformed R2 specimen and the most elongated R2 specimen, and the results are shown in Fig. 4. The 16Bit grey scale values of the tomograms were normalized by the reconstruction software, and span between 0 and 32000. For the elongated R2 specimen, the average value $\mu_\xi(r, z)$ of the grey-scale field, see Fig. 4f, indicates a marked reduction of density in the notched section of the specimen. According to Fig. 4c and g, the standard deviation $\sigma_\xi(r, z)$ is slightly higher in the notched section than for the material outside the notch. For the elongated R2 specimen, the higher coefficient of variation $C_{v\xi}(r, z)$ in the notched region is therefore caused both by the increased standard deviation $\sigma_\xi(r, z)$ and the lower average value $\mu_\xi(r, z)$. The standard deviation $\sigma_\xi(r, z)$ is comparable for the undeformed material and the background, indicating that the main source of variation is noise. Through regression, the variation in grey-scale value was found to be of Gaussian nature. The increased standard deviation $\sigma_\xi(r, z)$ for deformed material could be due to material in-homogeneity. However, as indicated by the coefficient of variation $C_{v\xi}(r, z)$, the deviation from axisymmetry is limited, and $\mu_\xi(r, z)$ is considered representative for the specimen for the purpose of this study. It should here be noted that the number of re-sampled pixels in the circumferential direction is proportional to the radial coordinate r, and statistical values calculated for small values of r, i.e. close to the center axis of the axisymmetric specimen, should therefore be treated with care.

A relative density field $\rho^*(r, z)$ was calculated by normalising $\mu_\xi(r, z)$ to the average grey scale value of undeformed material $\bar{\xi}$ and background ξ_0:

$$\rho^*(r, z) = \frac{\mu_\xi(r, z) - \xi_0}{\bar{\xi} - \xi_0} \tag{8}$$

where $\bar{\xi}$ was determined as the average grey scale value of a sub-frame covering a section of undeformed material, and ξ_0 was determined as the average grey scale value of a region outside of the specimen. The value of ξ_0 varies between samples, and the difference between the highest and lowest obtained value is in the order of 1% of the grey scale value of undeformed material $\bar{\xi}$.

The scans of the two undeformed specimens R20 and R2 were used to obtain an indication of the accuracy of the relative density measurements. These specimens should have a homogeneous density field, and the relative density is shown in Fig. 5. The relative density varies between 0.97 and 1.03, except in the vicinity of the upper notch shoulder of the R20 specimen, where a lower value of approx. 0.95 is found. For the R2 specimen, higher densities are estimated where the cross-section of the specimen is smaller.

Another indicator of the accuracy of the method is obtained by integrating the relative density fields of the notched section of the

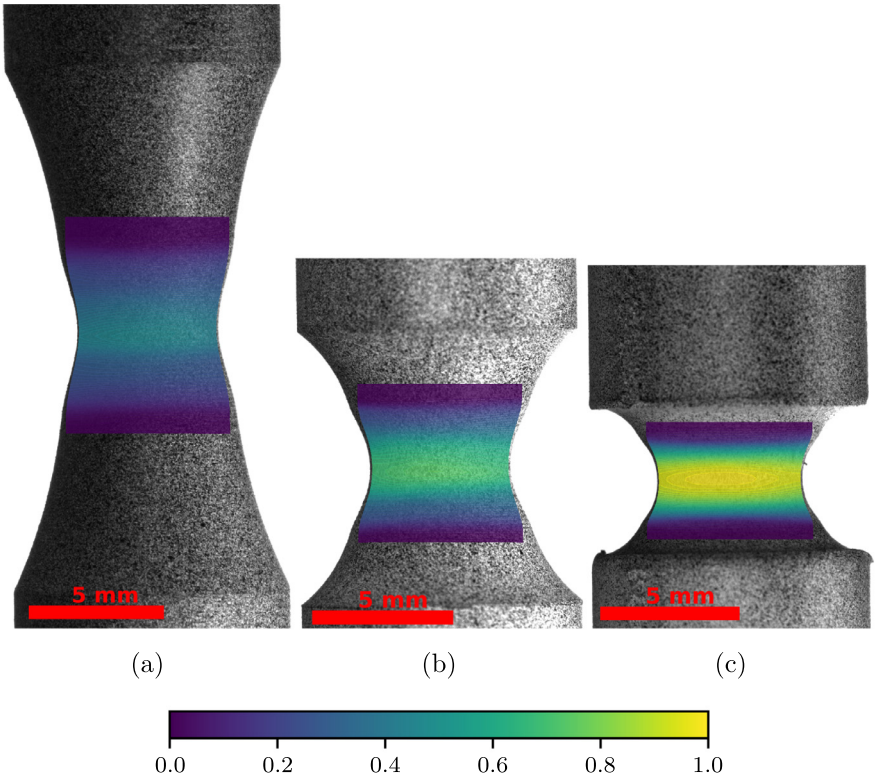

Fig. 9. Deformed state and true longitudinal strain field measured using DIC for specimens (a) R20, (b) R5, and (c) R2, deformed at nominal strain rate of 10^{-4} s^{-1}. The shown specimens are the ones deformed to the largest elongation of 2.5 mm. Note that as 2D DIC is used on circular specimens, the longitudinal strain is valid only in the notch root.

specimens with equal initial geometry. According to the principle of mass conservation, the integral of the density field within the notched section of a specimen in its undeformed state and of specimens deformed to 1.5 mm, 2.0 mm and 2.5 mm should yield the same value. The largest difference was found for the R2 specimens deformed at the highest strain rate, where a mass change of 2.5% was found between specimens.

For comparison with the average relative density estimates found from the surface (DIC) measurements described in Section 2.4.2, an average relative density $\bar{\rho}^*_{disc}$ for a disc through the cross-section of the notch at $z = 0$ is calculated as:

$$\bar{\rho}^*_{disc} = \frac{\sum_{i=1}^{M} \rho^*(r_i, 0) r_i}{\sum_{i=1}^{M} r_i} \tag{9}$$

where r_i is the radial position of the voxel, $\rho^*(r_i, 0)$ is the relative density at radial position i, and M is the number of pixels in the radial direction.

2.6. Validation by synchrotron radiation computed X-ray tomography (sr-XCT)

In order to investigate the contribution of beam-hardening in the tomograms acquired by the polychromatic home laboratory XCT scanner, some of the specimens were scanned using monochromatic synchrotron radiation computed tomography (sr-XCT). Thus, the R2 specimens elongated at a nominal strain rate of 10^{-4} s^{-1} were scanned at the TOMCAT beamline X02DA located at the Paul Scherrer Institute (PSI) (Stampanoni et al., 2006). An energy of 35 keV and a short specimen-sensor distance of 10 mm were used to ensure absorption contrast rather than phase contrast. The resulting voxel size was 3.25 μm. The same procedure as presented in Section 2.5 was used to calculate the relative density fields. A relative density field measured by sr-XCT is shown in Fig. 6. The spots seen in Fig. 6 are caused by dust on the scintilator during the experiment.

Fig. 7 shows a comparison of the relative density functions $\rho^*(r, 0)$ obtained by XCT and sr-XCT along the radial axis at the notch. As the sr-XCT and XCT scans have slightly different voxel sizes, the radial coordinates are normalized to the minimum cross-sectional radius R. The agreement is in general satisfactory, although sr-XCT gives a slightly higher density for the specimens strained to the two lowest deformation levels. Note that no homogeneous sample was scanned by sr-XCT. In Eq. (8), the reference grey scale $\bar{\xi}$ is taken from a section of the undeformed material for each tomogram. However, recalling from Fig. 5 that XCT of an un-deformed R2 specimen yields a 2% to 3% higher relative density where the cross-section of the specimen is smaller, one could argue that the reference grey scale $\bar{\xi}$ should be increased by 3% to account for this effect, and the consequence is shown with the shaded band in Fig. 7. It appears that the relative densities obtained with XCT coincide well with the sr-XCT measurements, thus indicating that there is no significant beam hardening.

3. Results

True stress-strain curves from the 18 tests are shown in Fig. 8. The repeatability of the experiments appears to be good. All curves have an initially linear loading phase followed by softening and subsequent hardening. The stress at which softening is initiated is observed to be dependent on the nominal strain rate, but little influence of notch root curvature is found. The notch root strain at maximum elongation increases with decreasing notch radius. Fig. 8 shows also that the true strain increases slightly during the first part of the unloading process. Deformed R20, R5 and R2 specimens with corresponding longitudinal true strain fields measured by DIC are shown in Fig. 9. The specimens depicted in the figure are all elongated to 2.5 mm.

The average relative density based on DIC as given by Eqs. (3) and

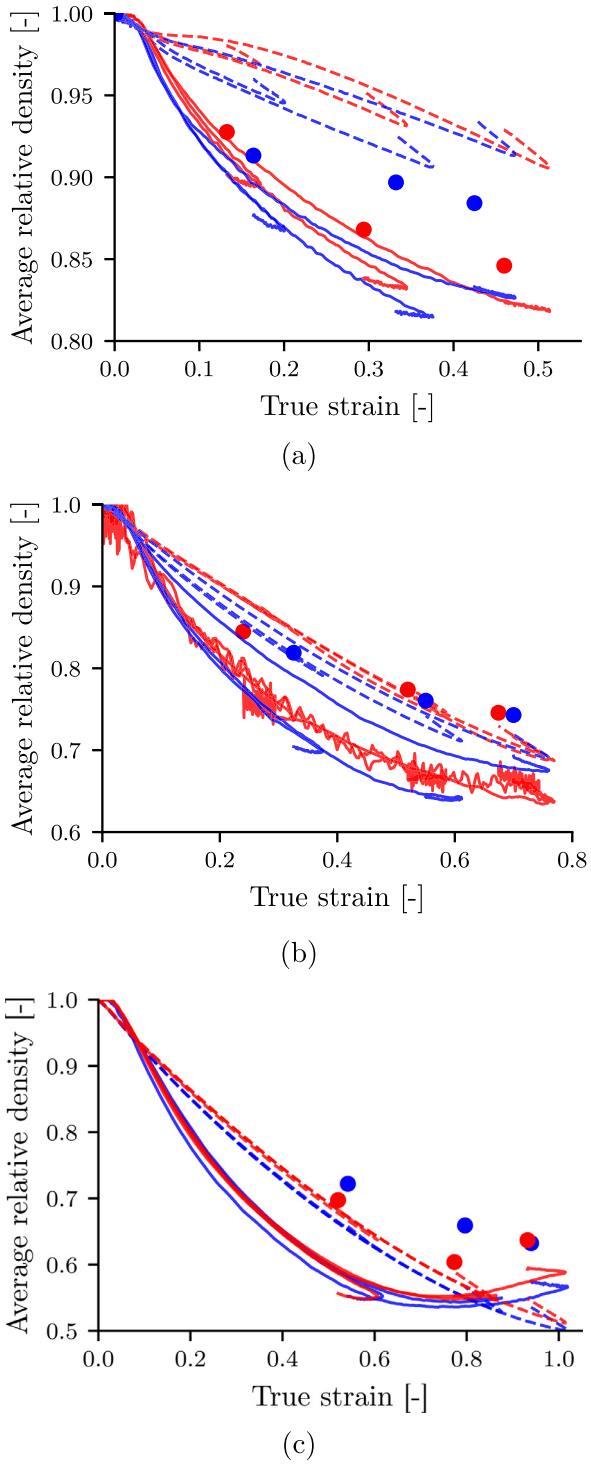

Fig. 10. Average relative density vs. true strain curves at two nominal strain rates of 10^{-4} s^{-1} (blue) and 10^{-3} s^{-1}(red) for specimens (a) R20, (b) R5, and (c) R2. Estimates by Eq. (3) are marked by dashed lines and Eq. (4) by solid lines. The dots are average relative densities determined from XCT using Eq. (9). (For interpretation of the references to colour in this figure legend, the reader is referred to the web version of this article.)

(4) is shown in Fig. 10. In both cases, the average relative density for a given strain decreases with decreasing notch radius. Application of Eq. (3) yields a close-to-linear decrease of the average relative density for all specimens, followed by a linear increase when unloaded. In contrast, Eq. (4) results in a non-linear evolution and lower average relative densities are predicted for all samples, whereas the increase of the average relative density during unloading is smaller.

The average relative densities calculated from the relative density fields obtained by XCT, see Eq. (9), are included as circular dots in Fig. 10. In the case of R20 specimens, the average relative densities based on XCT fall between the estimates using Eq. (4) and Eq. (3). For the R5 and R2 specimens, Eq. (3) has closer correspondence to the XCT-based estimates. Both Eq. (3) and Eq. (4) underestimate the average relative density obtained from XCT measurements for the R2 specimens.

Fig. 11 shows the relative density fields as determined with Eq. (8) after unloading of the samples deformed at a nominal strain rate of 10^{-4} s^{-1} to all three levels of elongation. The corresponding fields for a nominal strain rate of 10^{-3} s^{-1} are shown in Fig. 12. The relative density fields are similar for the two applied nominal strain rates, and the following findings refer to specimens deformed at both rates. An interesting observation is that the zone with the lowest relative density is found near the symmetry axis for the R20 and R5 specimens, whereas it is located closer to the notch surface for the R2 specimens. It appears also that the relative density within the notch region of the specimen decreases with increasing deformation for all samples. Tomograms for the R2 and R5 specimens and the material points at the surface as found with DIC reveal that the region with reduced relative density at 1.5 mm elongation (sub-figures d,g) does not spread into new material with increasing deformation. Instead, these regions are stretched at 2.0 mm and 2.5 mm elongation (sub-figures respectively e,h and f,i). Simultaneously, the relative density decreases within these regions. On the other hand, there is a larger tendency to reduction of density into new regions with increasing deformation for the R20 sample.

The relative density distribution along the radial axis is shown in Fig. 13 for the three deformation states at a nominal strain rate of 10^{-4} s^{-1}. The corresponding distributions at a strain rate of 10^{-3} s^{-1} are shown in Fig. 14. The R20 and R5 specimens show a monotonically increasing relative density towards the surface of the notch. The R2 specimens have an approximately constant relative density in the interior of the specimen, whereas it increases rapidly in the vicinity of the notch root.

4. Discussion

The true stress vs. true strain curves in Fig. 8 are similar to measurements presented by Olufsen et al. (2019) for the same material. The stress at which softening is initiated was found to be similar for the different stress triaxiality ratios, demonstrating the pressure sensitive nature of the material. Pronounced dilation is anticipated for this material (Olufsen et al., 2019), initiated by decohesion of particles from the surrounding matrix material. A possible reason for the pressure sensitivity of the material could therefore be a coupling between particle decohesion and the triaxiality of the stress state.

An increasing true strain is observed in the first part of the unloading process in Fig. 8, indicating a viscous material behavior. For the R5 and R20 specimens, the strain at which unloading is initiated varies between the two nominal strain rates. Recall that the same machine displacement was used across both strain rates, thus, the differences in strain at unloading are attributed to viscous material behavior. Except for the most elongated R20 specimen, the true strain at the start of the unloading process is larger at the low rate than the high nominal strain rate for all R5 and R20 specimens, indicating less pronounced strain localization at the high rate. This observation is supported by Fig. 10, which shows that the average relative density indeed is slightly smaller at the low nominal strain rate of 10^{-4} s^{-1}, implying somewhat larger dilation and hence more localized deformation. For the R2 specimens, similar strains are observed at unloading for both strain rates.

The accuracy of the XCT measurements was assessed by comparison to experimental data obtained by sr-XCT. A voxel size of 3.25 μm was used for the sr-XCT scans, and individual voids were therefore not resolved. Any information related to void morphology is therefore not

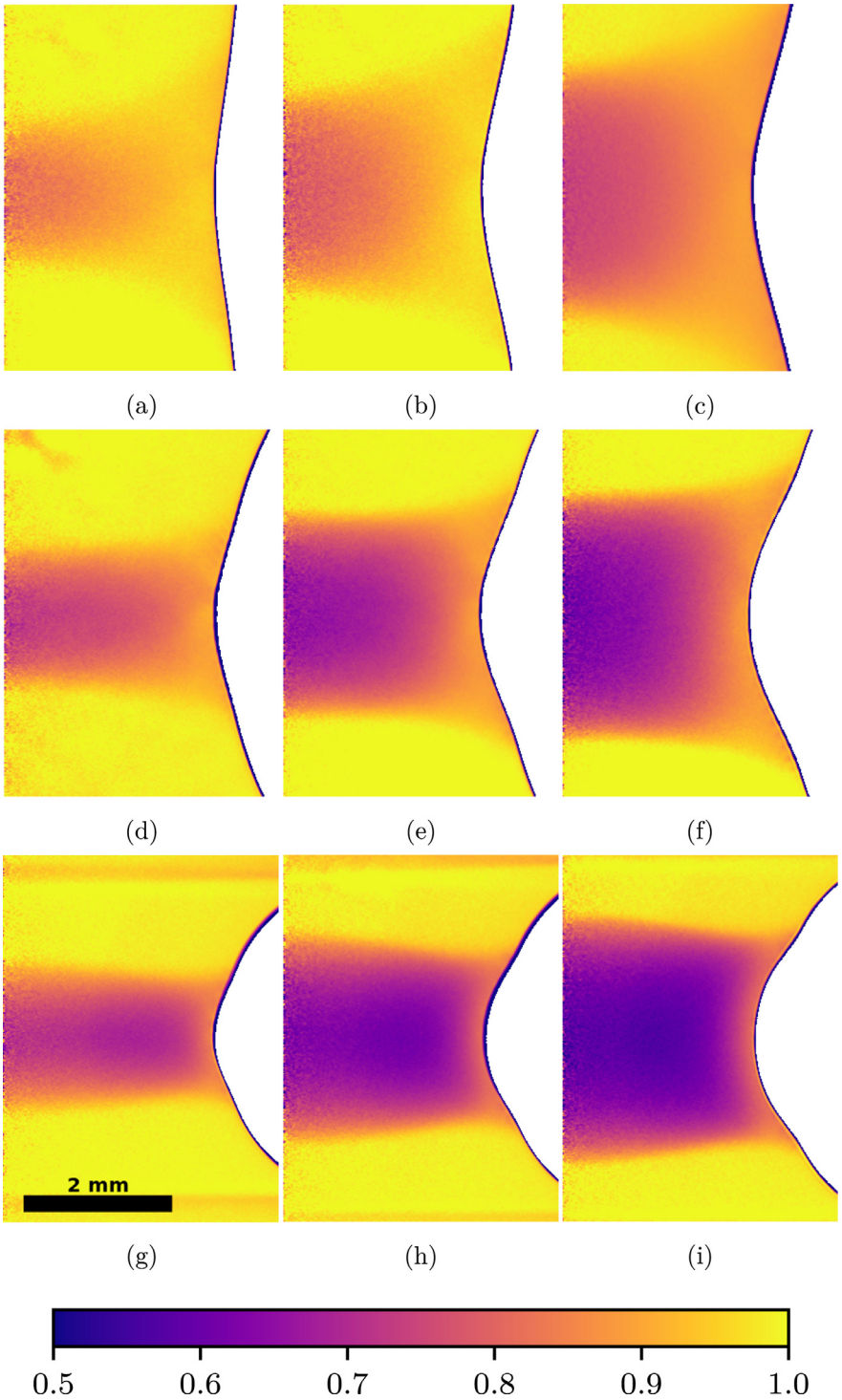

Fig. 11. Relative density fields obtained with Eq. (8) for R20 (a, b, c), R5 (d, e, f) and R2 (g, h, i) specimens at three elongations of 1.5 mm (a, d, g), 2.0 mm (b, e, h) and 2.5 mm (c, f, i), at a nominal strain rate of 10^{-4} s^{-1}. The background has been removed from the images, causing the black contour line.

obtained from the sr-XCT scans. It appears from Fig. 7 that the density variations are one order of magnitude larger than the difference between sr-XCT and XCT measurements. As the error source of beam hardening is avoided in sr-XCT, the consistency between the relative density measurements using monochromatic sr-XCT and polychromatic XCT demonstrates that the relative density estimates acquired by XCT are sufficiently accurate for the purpose of this study. Another check of the accuracy of the XCT measurements is obtained by integrating the relative density fields within the notch section of the R2 specimens. The largest deviation in mass was found to be 2.5% relative to an undeformed specimen. In addition to the error sources discussed earlier, deviation in mass could be caused by inaccuracies in the manufacturing process of the specimens or inaccuracies in the identification of the neck shoulder.

The estimates of the average relative density ρ^*_{disc} obtained by Eq. (4) are lower than those obtained by Eq. (3). The reason for this is that the increase of the notch curvature induced by additional necking of the specimen is included only in Eq. (4), which assumes that the longitudinal stretch distribution along the radial axis of the specimen can be described by a second-degree polynomial. This assumption may not

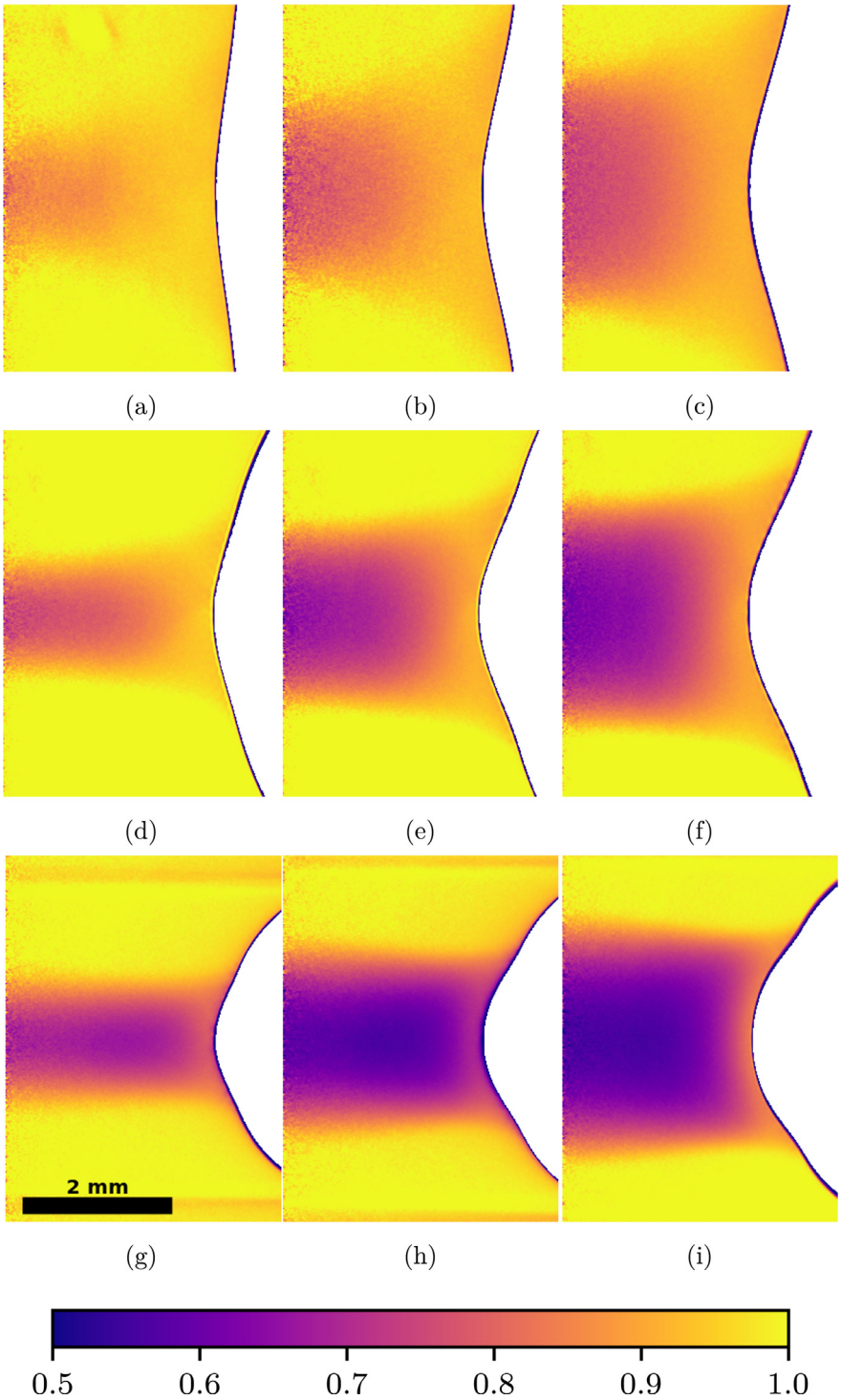

Fig. 12. Relative density fields obtained with Eq. (8) for R20 (a, b, c), R5 (d, e, f) and R2 (g, h, i) specimens at three elongations of 1.5 mm (a, d, g), 2.0 mm (b, e, h) and 2.5 mm (c, f, i), at a nominal strain rate of 10^{-3} s^{-1}. The background has been removed from the images, causing the black contour line.

hold for all specimen geometries and materials (Laiarinandrasana et al., 2016), a finding supported by the relative density distributions shown in Fig. 13. Axisymmetry is explicitly assumed in Eq. (4) and Eq. (3), and was verified by comparing the radial stretch extracted from the two orthogonal cameras, showing close correspondence.

The initial specimen geometry influences how the density in the notch region changes as the specimen is deformed. For a smaller notch radius, a lower relative density is observed for a given strain, due to the increased stress triaxiality ratio. Such a coupling between notch radius and the tendency of a material to dilate has been reported in numerous studies, see for example (Ognedal et al., 2014b; Olufsen et al., 2019; Boisot et al., 2011).

According to Figs. 13 and 14, a relative density less than unity is observed close to the specimen surface for all specimens, suggesting that material dilation is present even at low triaxiality ratios. Material dilation at the specimen surface conforms to the frequent observation of ”stress whitening” of deformed polymers (G’Sell et al., 2002). Due to the white color of the material, however, stress whitening cannot be easily identified in this study.

From Figs. 13 and 14, it can be seen that the relative density close to

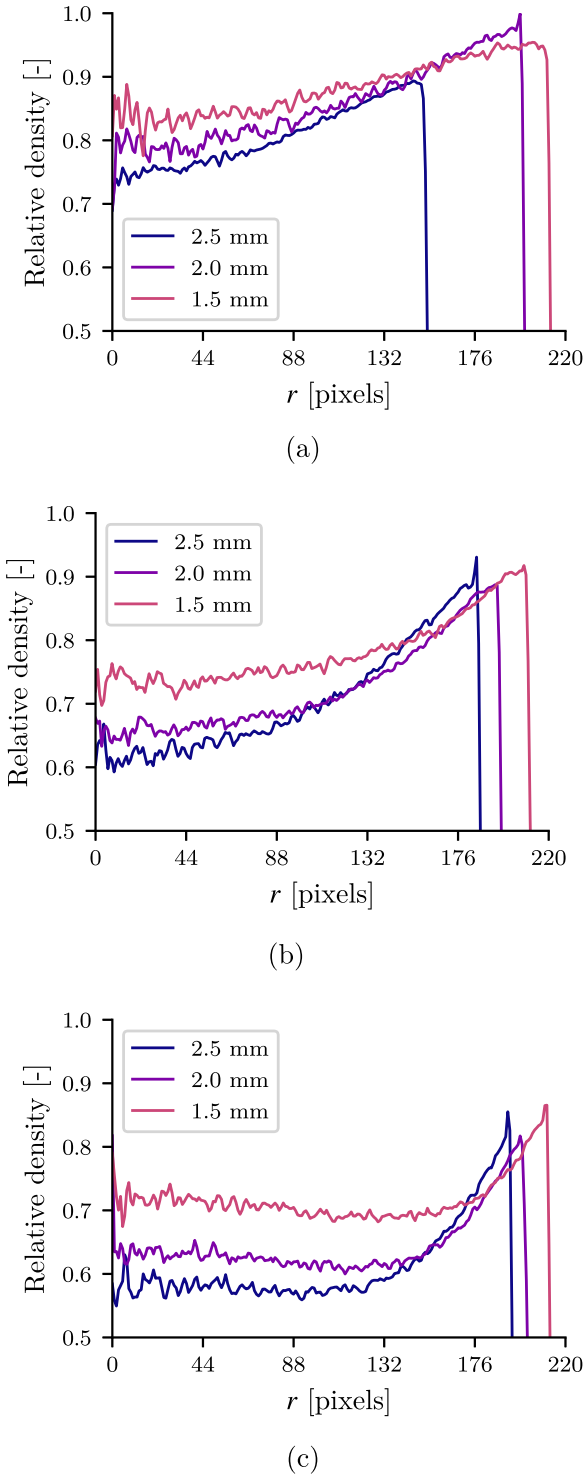

Fig. 13. Radial relative density distribution for the (a) R20, (b) R5 and (c) R2 specimens deformed to three elongations at a nominal strain rate of 10^{-4} s^{-1}.

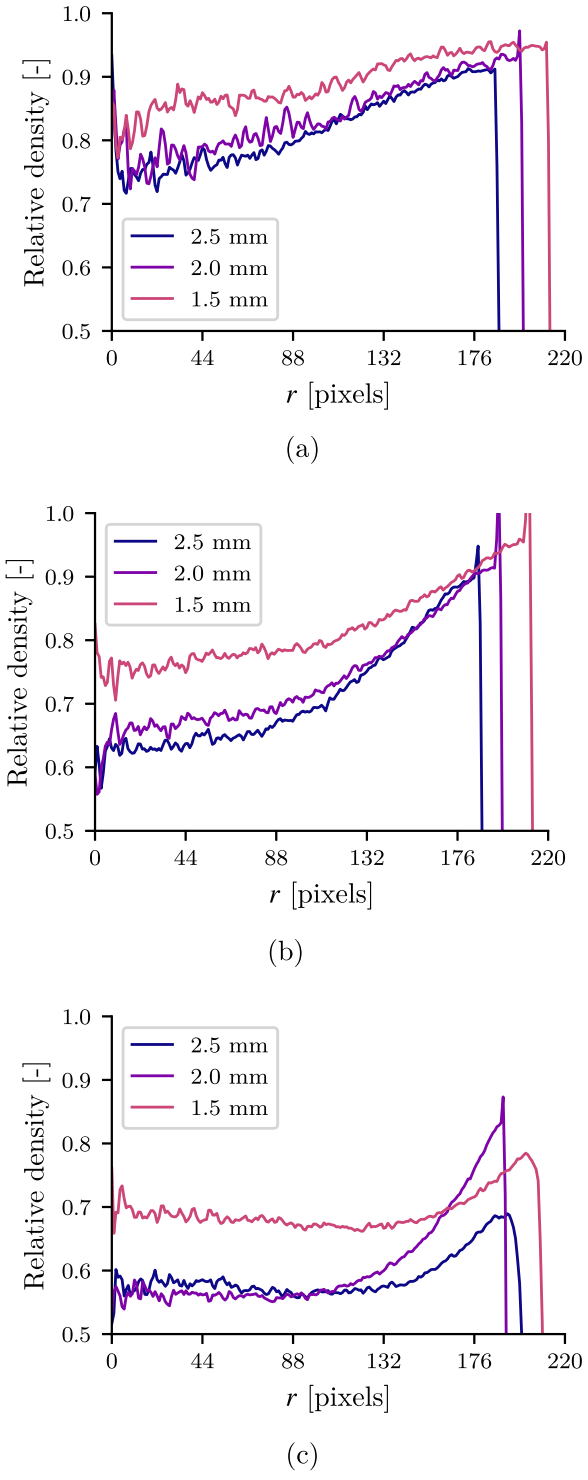

Fig. 14. Radial relative density distribution for the (a) R20, (b) R5 and (c) R2 specimens deformed to three elongations at a nominal strain rate of 10^{-3} s^{-1}.

the surface of the specimen does not always decrease monotonically for increasing elongation. A possible reason for this observation is that the individual curves are from unique specimens with their inherent variations.

For the R2 and R5 specimens, the region with reduced density in Figs. 11 and 12 appears to be confined to the same material points even for increasing deformation. One possible explanation for this observation is that the cross-section area increases rapidly outside the notch root. Another cause might be the high stress triaxiality ratio in the origin of the notch.

An elastic contribution to the average relative density is observed during unloading for all specimens, see Fig. 10. This contribution has also been observed experimentally by Brusselle-Dupend et al. (2011), where PVF2 was investigated using circular notched tensile specimens that were unloaded after large deformations. As the tomograms in the present study are acquired on unloaded specimens, the elastic contribution to the average relative density is not captured herein. However, the contribution of elasticity to the total average relative density

appears to be limited and the deviation between the surface based average relative density and the average relative density estimates from XCT cannot be fully explained by the presence of an elastic contribution to the average relative density. When detecting the presence of material dilation is of interest, the surface based methods are applicable. However, as the degree of correspondence between the $\bar{\rho}^*_{disc}$ from XCT and the surface based ρ^*_{disc} estimates appears to be dependent on the geometry of the specimen, quantitative results should be interpreted with caution.

Stress triaxiality has been identified as one of the factors governing the dilation of polymers (Boisot et al., 2011; Ognedal et al., 2014b; Olufsen et al., 2019). However, quantitative values of the stress triaxiality distribution in a dilating tensile specimen call for finite element analysis (Boisot et al., 2011), being out of the scope of this study. An analytic expression for stress triaxiality within an axisymmetric notched specimen is made available by the Bridgman formula and predicts a parabolic distribution of the stress triaxiality ratio. However, the Bridgman formula assumes isochoric, pressure insensitive and rate independent plasticity, and all these assumptions are violated for the PVC studied here.

5. Conclusions

It is here demonstrated by means of X-ray computed tomography that a large reduction of relative density and hence pronounced dilation is present during the deformation of axisymmetric notched tensile specimens made of mineral-filled PVC.

The general observation from the XCT measurements is that the relative density decreases with straining for all investigated specimens, and a smaller notch radius promotes material dilation. The shape of the relative density distribution within the notch region is shown to be dependent on the specimen geometry. The density distribution in the R2 specimens has an approximately constant value in the core of the specimen, increasing in the vicinity of the notch root. For the R5 and R20 specimens, the density is lowest in the center of the specimen and rises monotonically towards the notch root.

Estimating the average relative density of a disc through the minimum cross-section of the notch based on surface deformations does not reproduce the estimates obtained by XCT. Surface deformation-based average relative density estimates should, therefore, be treated with caution and considered as qualitative measures.

Given the appropriate precautions, tomograms acquired by the polychromatic home laboratory XCT scanner can give close correspondence to density estimates obtained by a monochromatic synchroton (sr-XCT). The axisymmetric nature of the tomograms can be exploited, resulting in relative density measurements with a reduced noise level. This opens for future mechanical tests with in-situ XCT scanning.

Declaration of Competing Interest

The authors declare that they have no known competing financial interests or personal relationships that could have appeared to influence the work reported in this paper.

Acknowledgements

We are thankful to Mr Trond Auestad for the invaluable help with the experimental set-up and performing the tensile testing. We also acknowledge Dr Anne Bonnin at the Paul Scherrer Institute for performing the sr-XCT scans and valuable discussion. The authors gratefully appreciate the financial support from the Research Council of Norway through the center for Advanced Structural Analysis, Project No. 237885 (SFI-CASA). The use of the X-ray laboratory at the Department of Physics at NTNU, partially financed by the Norwegian Research Council through project no. 208896, is acknowledged. DWB thanks the Research Council of Norway through its Centres of Excellence funding scheme, project number 262644.

Supplementary material

Supplementary material associated with this article can be found, in the online version, at 10.1016/j.mechmat.2019.103296

References

Andersen, M., 2016. An Experimental and Numerical Study of Thermoplastics at Large Deformations. Ph.D. thesis.
Andersen, M., Hopperstad, O.S., Clausen, A.H., 2019. Volumetric strain measurement of polymeric materials subjected to uniaxial tension. Strain (April), e12314. https://doi.org/10.1111/str.12314.
Bergström, J., 2015. Mechanics of Solid Polymers. Elsevierhttps://doi.org/10.1016/B978-0-323-31150-2.00002-9.
Bø Fløystad, J., Skjønsfjell, E.T.B., Guizar-Sicairos, M., Høydalsvik, K., He, J., Andreasen, J.W., Zhang, Z., Breiby, D.W., 2015. Quantitative 3D X-ray imaging of densification, delamination and fracture in a micro-composite under compression. Adv. Eng. Mater. 17 (4), 545–553. https://doi.org/10.1002/adem.201400443.
Boisot, G., Laiarinandrasana, L., Besson, J., Fond, C., Hochstetter, G., 2011. Experimental investigations and modeling of volume change induced by void growth in polyamide 11. Int. J. Solids Struct. 48 (19), 2642–2654. https://doi.org/10.1016/j.ijsolstr.2011.05.016.
Brusselle-Dupend, N., Rosenberg, E., Adrien, J., 2011. Characterization of cavitation development while tensile testing PVF2 using 3D X-ray microtomography. Mater. Sci. Eng. A 530 (1), 36–50. https://doi.org/10.1016/j.msea.2011.09.009.
Diaz, A., Trtik, P., Guizar-Sicairos, M., Menzel, A., Thibault, P., Bunk, O., 2012. Quantitative x-ray phase nanotomography. Phys. Rev. B - Condensed Matter Mater. Phys. 85 (2), 1–4. https://doi.org/10.1103/PhysRevB.85.020104.
Esmaeili, M., Fløystad, J.B., Diaz, A., Høydalsvik, K., Guizar-Sicairos, M., Andreasen, J.W., Breiby, D.W., 2013. Ptychographic X-ray tomography of silk fiber hydration. Macromolecules 46 (2), 434–439. https://doi.org/10.1021/ma3021163.
G'Sell, C., Hiver, J.M., Dahoun, A., 2002. Experimental characterization of deformation damage in solid polymers under tension, and its interrelation with necking. Int. J. Solids Struct. 39 (13–14), 3857–3872. https://doi.org/10.1016/S0020-7683(02)00184-1.
Hsieh, J., 2015. Computed tomography: Principles, design, artifacts, and recent advances. SPIEhttps://doi.org/10.1117/3.2197756.
Johnsen, J., Grytten, F., Hopperstad, O.S., Clausen, A.H., 2017. Influence of strain rate and temperature on the mechanical behaviour of rubber-modified polypropylene and cross-linked polyethylene. Mech. Mater. 114, 40–56. https://doi.org/10.1016/j.mechmat.2017.07.003.
Laiarinandrasana, L., Klinkova, O., Nguyen, F., Proudhon, H., Morgeneyer, T.F., Ludwig, W., 2016. Three dimensional quantification of anisotropic void evolution in deformed semi-crystalline polyamide 6. Int. J. Plast. 83, 19–36. https://doi.org/10.1016/j.ijplas.2016.04.001.
Laiarinandrasana, L., Morgeneyer, T.F., Proudhon, H., N'Guyen, F., Maire, E., 2012. Effect of multiaxial stress state on morphology and spatial distribution of voids in deformed semicrystalline polymer assessed by X-ray tomography. Macromolecules 45 (11), 4658–4668. https://doi.org/10.1021/ma3005247.
Maire, E., Withers, P.J., 2014. Quantitative X-ray tomography. Int. Mater. Rev. 59 (1), 1–43. https://doi.org/10.1179/1743280413Y.0000000023.
Ognedal, A.S., Clausen, A.H., Berstad, T., Seelig, T., Hopperstad, O.S., 2014. Void nucleation and growth in mineral-filled PVC - an experimental and numerical study. Int. J. Solids Struct. 51 (7–8), 1494–1506.
Ognedal, A.S., Clausen, A.H., Dahlen, A., Hopperstad, O.S., 2014. Behavior of PVC and HDPE under highly triaxial stress states: an experimental and numerical study. Mech. Mater. 72, 94–108.
Ognedal, A.S., Clausen, A.H., Polanco-Loria, M., Benallal, A., Raka, B., Hopperstad, O.S., 2012. Experimental and numerical study on the behaviour of PVC and HDPE in biaxial tension. Mech. Mater. 54, 18–31. https://doi.org/10.1016/j.mechmat.2012.05.010.
Olufsen, S., Clausen, A.H., Hopperstad, O.S., 2019. Influence of stress triaxiality and strain rate on stress-strain behaviour and dilation of mineral-filled PVC. Polym. Test 75, 350–357. https://doi.org/10.1016/j.polymertesting.2019.02.018.
Poulet, P.A., Hochstetter, G., King, A., Proudhon, H., Joannès, S., Laiarinandrasana, L., 2016. Observations by in-situ X-ray synchrotron computed tomography of the microstructural evolution of semi-crystalline polyamide 11 during deformation. Polym. Test 56, 245–260. https://doi.org/10.1016/j.polymertesting.2016.10.023.
Rossi, M., Genovese, L.C.K., Nalli, A.L.F., 2018. Evaluation of Volume Deformation from Surface DIC Measurement. D. pp. 1181–1194.
Schindelin, J., Arganda-Carreras, I., Frise, E., Kaynig, V., Longair, M., Pietzsch, T., Preibisch, S., Rueden, C., Saalfeld, S., Schmid, B., Tinevez, J.Y., White, D.J., Hartenstein, V., Eliceiri, K., Tomancak, P., Cardona, A., 2012. Fiji: an open-source platform for biological-image analysis. Nat. Methods 9 (7), 676–682. https://doi.org/10.1038/nmeth.2019.
Stampanoni, M., Groso, A., Isenegger, A., Mikuljan, G., Chen, Q., Bertrand, A., Henein, S., Betemps, R., Frommherz, U., Böhler, P., Meister, D., Lange, M., Abela, R., 2006. Trends in synchrotron-based tomographic imaging: the SLS experience (September) 2006, 63180M. doi:10.1117/12.679497.
Sutton, M.A., Orteu, J.-J., Schreier, H.W., 2009. Image Correlation for Shape, Motion and Deformation Measurements. 53https://doi.org/10.1017/CBO9781107415324.004.